ELMs and Constraints on the H-Mode Pedestal: A Model Based on Peeling-Ballooning Modes

P.B. Snyder[1)], H.R. Wilson[2)], J.R. Ferron[1)], L.L. Lao[1)], A.W. Leonard[1)], D. Mossessian[3)], M. Murakami[4)], T.H. Osborne[1)], A.D. Turnbull[1)], X.Q. Xu[5)]

[1)]General Atomics, P.O. Box 85608, San Diego, California 92186-5608, USA
[2)]EURATOM/UKAEA Fusion Association, Culham Science Centre, Abingdon, Oxon UK
[3)]Massachusetts Institute of Technology PSFC, Cambridge, Massachusetts 02139, USA
[4)]Oak Ridge National Laboratory, Oak Ridge, Tennessee, USA
[5)]Lawrence Livermore National Laboratory, Livermore, California 94550, USA
email contact of main author: snyder@fusion.gat.com

Abstract We propose a model for Edge Localized Modes (ELMs) and pedestal constraints based upon theoretical analysis of instabilities which can limit the pedestal height and drive ELMs. The sharp pressure gradients, and resulting bootstrap current, in the pedestal region provide free energy to drive peeling and ballooning modes. The interaction of peeling-ballooning coupling, ballooning mode second stability, and finite-Larmor-radius effects results in coupled peeling-ballooning modes of intermediate wavelength generally being the limiting instability. A highly efficient new MHD code, ELITE, is used to calculate quantitative stability constraints on the pedestal, including constraints on the pedestal height. Because of the impact of collisionality on the bootstrap current, these pedestal constraints are dependant on the density and temperature separately, rather than simply on the pressure. A model of various ELM types is developed, and quantitatively compared to data. A number of observations agree with predictions, including ELM onset times, ELM depth, and variation in pedestal height with collisionality and discharge shape. Stability analysis of series of model equilibria are used both to predict and interpret pedestal trends in existing experiments and to project pedestal constraints for future burning plasma tokamak designs.

1. Introduction & Motivation

High performance ("H-mode") operation in tokamaks is characterized by the spontaneous formation of a transport barrier near the edge of the closed flux surface region. The term "pedestal" is used here to describe the resulting sharp pressure gradient region just inside the magnetic separatrix in H-mode operation. This region generally occupies approximately the outer 1-5% in normalized radius of the closed flux surface region, but is observed to have a disproportionately large impact on overall plasma performance [see e.g., Refs. 1-3].

The physics of the pedestal is important to the performance of present tokamak experiments, and expected to be critically important for future burning plasma devices, for two primary reasons. The first is the strong dependence, both observed and predicted by transport models, of core confinement on the pressure at the top of the pedestal (or "pedestal height"). Core transport models generally take the pedestal height as an input parameter, and predict the resulting transport in the core plasma. Because these models are generally "stiff" (transport increases rapidly above a critical gradient), the predicted core temperature, and hence fusion power or $Q=P_{fus}/P_{in}$, increases strongly with increasing pedestal height. For GLF23, the dependence is roughly $P_{fus}\sim\beta^2_{ped}$, where β_{ped} is the ratio of plasma to magnetic pressure at the top of the pedestal [4]. Hence, transport code predictions for proposed burning plasma candidates can be restated in terms of the pedestal height (or at a given density, the pedestal temperature) requirements for a given level of fusion performance.

The second important pedestal physics issue is the presence of edge localized modes (ELMs). ELMs are repetitive magnetic perturbations in the pedestal vicinity, which transport bursts of particles, and usually also heat, across the separatrix and to the divertor plates [see e.g., Refs. 5-9]. While the ELMs themselves are generally benign in present experiments, large ELMs potentially pose a significant divertor erosion risk in burning plasma scale devices. Furthermore, as discussed below, ELMs appear to be a manifestation of magnetohydrodynamic instabilities driven by a combination of the strong pressure gradient and resulting bootstrap current in the pedestal region. These instabilities place constraints on the achievable pedestal height at a given transport barrier width, and thus constrain overall performance as discussed above. Developing a predictive understanding of the physics

controlling ELMs and the pedestal height is thus an important objective for pedestal theory, with a goal of maximizing the pedestal height while maintaining acceptable ELM behavior.

2. Pedestal MHD Stability and the ELITE Code

The sharp pressure gradients, and consequent large bootstrap currents in the pedestal region can destabilize peeling (ie edge localized external kink) and ballooning modes over a wide range of toroidal mode numbers (n). The bootstrap current plays a complex dual role in the stability physics, on one hand driving peeling modes, while on the other lowering edge shear and opening second stability access to high-n ballooning modes. Field line bending stabilizes long wavelength modes, while short wavelengths are stabilized by a combination of second stability and FLR/diamagnetic effects, shifting the limiting modes to intermediate wavelengths (typically n~4-40). These dominant modes are referred to here as coupled ``peeling-ballooning'' modes, and are driven by both parallel current (J_{ped}) and the pressure gradient (p'_{ped}) [10,11]. These intermediate-n peeling-ballooning modes impose constraints on the pedestal height, which are functions of the pedestal width, plasma shape, collisionality, safety factor and other equilibrium details.

A new MHD stability code, ELITE [12,11], employs a novel finite-n extension of ballooning theory [12] which allows accurate and highly efficient study of $5 \lesssim n \lesssim 100$ peeling-ballooning modes in shaped toroidal geometry. ELITE calculates both growth rates (compressionless or compressional) and mode structures of the limiting instabilities, which provide useful input for the development of ELM models. ELITE uses a Fourier representation in the poloidal direction, and employs numerical methods which allow very efficient stability calculations, facilitating its use in the large number of stability calculations which are needed to characterize pedestal stability constraints as a function of mode wavelength, pedestal width, plasma shape, collisionality, safety factor etc. A sample ELITE benchmark is shown in Figure 1, where growth rates from ELITE are compared at lower n's to growth rates from the GATO [13] code, and calculated mode structures are also compared. ELITE, together with low-n MHD codes such as GATO, allows quantitative study of the full relevant spectrum of n.

ELITE results together with analytic insights are used to develop a model of various types of ELMs and stability constraints on the pedestal, including direct constraints on the pedestal temperature (T_{ped}) [14]. Quantitative stability limits are calculated by varying the pedestal temperature and density, while self-consistently calculating the current, including bootstrap contributions. Figure 2(a) shows such limits for a JET-like equilibrium with fixed profile shapes. The stability boundary in J_{ped},β_N ($\beta_N \propto p'_{ped}$) space is shown for the range $5<n<30$, along with eigenmode structures of the limiting instability in various regimes. Peeling modes are the limiting instability at high J_{ped}, low p'_{ped}, while ballooning modes are most unstable at high p'_{ped}, low J_{ped}. Intermediate $6<n<8$ coupled peeling-ballooning modes are the limiting instability in the high p'_{ped}, high J_{ped} region in which high performance shots generally operate.

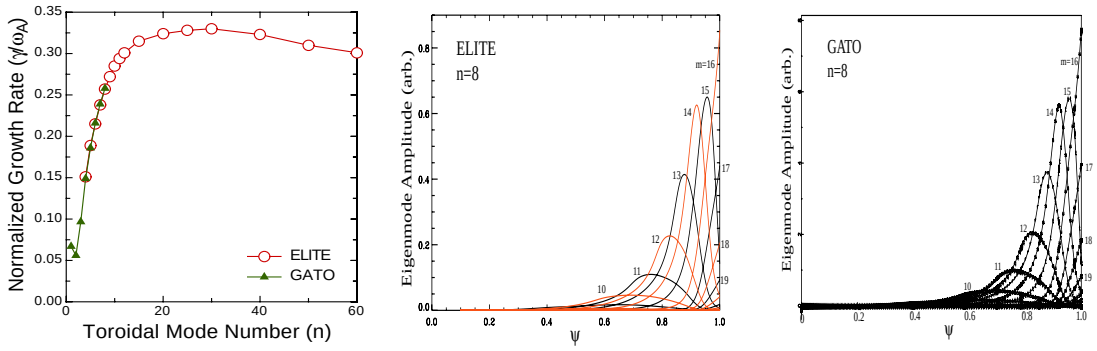

Fig. 1. (a) Growth rates from the ELITE and GATO codes for a circular benchmark case show good agreement in the range of overlap ($4 \le n \le 9$). Calculated eigenmode structures from (b) ELITE and (c) GATO are also compared. The relative amplitudes and radial structure for the various poloidal modes are shown here for n=8.

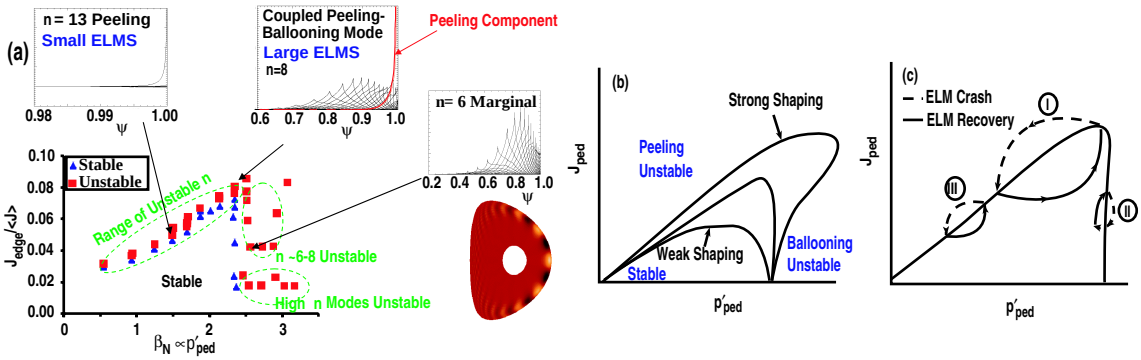

Fig. 2. (a) Calculated pedestal stability boundary for 5<n<30, along with eigenmodes of the limiting instability in various regimes. A 2D contour plot of an n=6 mode structure is inset. (b) A schematic showing the variation of pedestal stability boundaries with discharge shaping. (c) Model of 3 types of ELM cycle.

Because of the strong collisionality dependence of the bootstrap current, there is generally a monotonic relationship between the pedestal temperature and J_{ped} in the regime of interest. Hence, diagrams like Fig. 2(a) can be recast into stability limits in p'_{ped},T_{ped} space and used to calculate direct stability limits on the pedestal temperature at a given pedestal width. The pedestal stability boundary is a strong function of discharge shape, as shown schematically in Fig. 2(b). Improving shaping, for example by increasing triangularity, decouples peeling and ballooning modes, opening up second stability access for high-*n* modes, and leading to a stability boundary at higher p'_{ped}, J_{ped} (and hence higher T_{ped}). Note the rather complex dependencies depicted in Fig. 2(b). For example, while increasing current is always destabilizing for the "weakly shaped" case, it can be strongly stabilizing in a "strongly shaped" case where higher current lowers the shear and opens second stability access to high-n modes, resulting in a higher stability boundary in p'_{ped} and a longer wavelength limiting instability.

Models for various ELM cycles can be envisioned in this p'_{ped}, J_{ped} parameter space, as shown in Fig. 2(c). Dynamically, the pressure gradient increases on a transport time scale while the current grows on a slower resistive time scale, and an intermediate-n peeling-ballooning mode is triggered when the stability boundary is reached at the upper right of the diagram, resulting in a Type I ELM. Smaller ELMs are expected when the current, due to a combination of high collisionality and/or increased stability limit due to strong shaping, does not reach the peeling-ballooning limiting value, even in steady state. This small ELM cycle is labeled "II" in Fig. 2(c). At low power and low density, the small ELM cycle labeled "III" occurs (note that high density Type III ELMs are likely resistive modes). The ELM model takes the lost ELM energy to be related to the radial width of the calculated most unstable mode, and this, along with the location in parameter space at which the instability occurs, provides an explanation for large observed variations in ELM behavior. Of course nonlinear ELM physics and scrape-off-layer transport must be considered for the development of a fully quantitative theory of ELM heat loads to the divertor.

3. Comparison to Experiment and Projection to Future Devices

The peeling-ballooning stability model can be compared to experimental results in two ways: 1) via direct comparison with detailed equilibrium reconstructions of particular experimental shots, as described in Sec. 3.1, and 2) via comparison of the broad experimental database with stability trends predicted using series of model equilibria which systematically vary pedestal parameters as described in Sec. 3.2. Series of model equilibria can also be used to predict pedestal constraints in future machines, as described in Sec. 3.3.

3.1 Direct Comparisons to Experiment

Recent advances in high resolution pedestal diagnostics allow for detailed comparisons of the model with a range of experimental measurements. Figure 3 shows results of a case study in which the onset time of ELMs in DIII-D H mode shot 97887 is

compared to expectations from stability calculations. A time series of experimental equilibria are reconstructed, and stability is evaluated with ELITE at each time. As shown in Fig. 2a, the first ELM pulse reaches the divertor at t~2240ms, shortly after the calculated peeling-ballooning growth rate rises to a significant value, consistent with peeling-ballooning modes triggering the ELM. A further consistency check is provided by comparing the observed "depth" of the ELM, assessed by a statistical analysis of Thomson scattering data [Fig. 3(b)], with the calculated width of the most unstable (n=10) peeling-ballooning mode [Fig. 3(c)]. The poloidal structure of the mode is shown in an inset in Fig. 3(c), and we note that this characteristic structure, localized to the outboard side, is consistent with recent observations in divertor balance experiments on DIII-D [15].

It has been consistently observed on several tokamaks that both the pedestal pressure and the size of ELMs is reduced as density is increased [e.g. Ref 16]. To compare this observation to the stability model, experimental DIII-D equilibria are reconstructed at times shortly before an observed ELM, for low (shot 105999, n_{eped}~$2\bullet10^{19}m^{-3}$), medium (106005, n_{eped}~$4\bullet10^{19}m^{-3}$), and high (106007, n_{eped}~$6\bullet10^{19}m^{-3}$) density cases. Stability and predicted mode structure are then calculated with ELITE. Normalized growth rates as a function of toroidal mode number are shown in Fig. 4. In each case, the growth rate has reached a significant value shortly before the ELM occurs, again consistent with peeling-modes triggering the ELM, even though the high density case has significantly lower pedestal pressure. The most unstable wavelength, defined to be the wavelength with largest growth rate normalized to the diamagnetic frequency (which for a given case is proportional to $n\omega_A$), decreases with density as shown in Fig. 4. Furthermore, the radial width of the most unstable mode decreases from ~8% of the poloidal flux in the low density case, to ~4% in the medium density case and ~2% in the high density case. This increase in most unstable mode number and decrease in mode radial extent with increasing density both lead to the expectation of smaller ELMs at high density. However, we again emphasize that precise quantification of ELM size likely requires detailed study of ELM and SOL dynamics.

Analysis of Alcator C-Mod discharges shows similarly that ELMs emerge when peeling ballooning modes go significantly unstable, while "enhanced D-alpha" shots are generally stable [17]. JT-60U discharges have also been studied, and "giant" ELMs are found to correlate with broad peeling-ballooning instabilities, while "grassy" ELMs are driven by instabilities with narrower mode structure [18].

3.2 Comparisons to Experiment using Model Equilibria

The comparisons to experiment described in the previous section provide rigorous tests of the ELM model, and useful interpretive information on pedestal and ELM behavior in experiments. However, such comparisons require detailed equilibrium reconstructions, and thus can most easily be applied to the interpretation of existing experiments rather than to prediction of behavior in present or future devices.

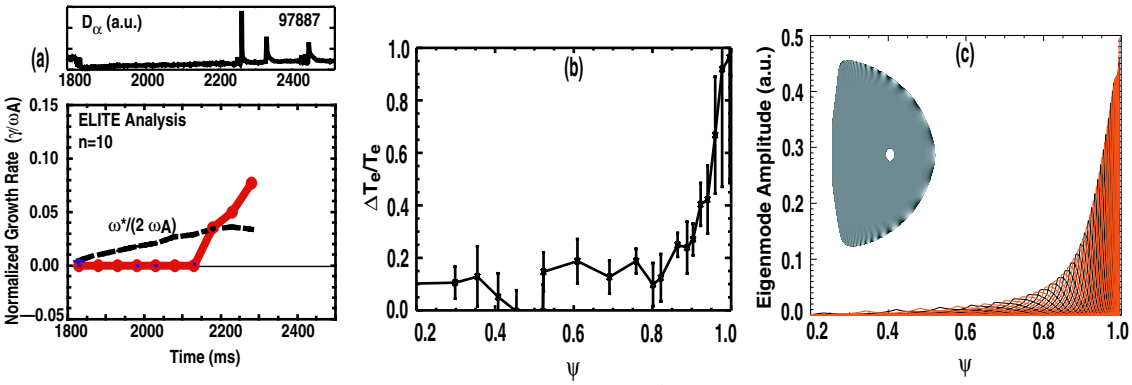

Fig. 3. Case study of ELMs in DIII-D shot 97887 (a) Above: D_α trace showing occurrence of the first ELM at t~2240ms. Below: Calculated growth rate of the most unstable (n=10) peeling-ballooning mode. (b) Observed $\Delta T_e/T_e$ from statistical analysis of Thomson scattering data provides a measure of the radial ELM penetration depth. (c) Calculated mode structure of n=10 peeling-ballooning mode at t=2230ms. A contour plot of the 2D mode structure is inset.

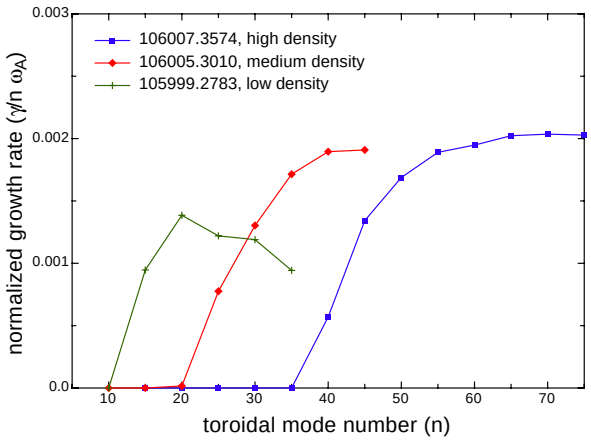

Fig. 4. Normalized growth rate vs. n, for DIII-D shots at high (106007), medium (106005), and low (105999) density, at times shortly before an ELM is observed. As density increases, the unstable spectrum peaks at shorter wavelengths.

In order to systematically predict pedestal trends, both in present and future devices, we construct series of model equilibria, varying important pedestal stability parameters, and calculating MHD stability with ELITE.

Model equilibria are constructed to match expected or measured global parameters, including the toroidal magnetic field (B_t), total plasma current (I_p), major radius (R), minor radius (a), average electron density ($\langle n_e \rangle$), plasma elongation (κ), and triangularity (δ). Density and temperature profiles are given a hyperbolic tangent shape in the pedestal [resembling measured profiles, see e.g. Refs. 3,1], and a simple polynomial dependence in the core:

$$n_e(\psi) = n_{sep} + a_{n0}\{\tanh[2(1-\Psi_{mid})/\Delta] - \tanh[2(\Psi-\Psi_{mid})/\Delta]\} + a_{n1}[1-(\Psi/\Psi_{ped})^{\alpha_{n1}}]^{\alpha_{n2}}$$

$$T(\psi) = T_{sep} + a_{T0}\{\tanh[2(1-\Psi_{mid})/\Delta] - \tanh[2(\Psi-\Psi_{mid})/\Delta]\} + a_{T1}[1-(\Psi/\Psi_{ped})^{\alpha_{T1}}]^{\alpha_{T2}}$$

where Ψ is the normalized poloidal flux, and Δ is the pedestal width in Ψ space. The constants a_0 and a_1 are chosen to give the desired pedestal and axis values, and α_1 and α_2 are chosen to approximately match expected core profiles from measurements or transport codes. Here we use $n_{ped}=0.71\langle n_e \rangle$, $n_0=1.1\langle n_e \rangle$, $n_{sep}=0.3\langle n_e \rangle$, $\alpha_{n0}=1$, $\alpha_{n1}=0.5$, $\alpha_{T0}=1$, $\alpha_{T1}=2$. In the pedestal region, the parallel current is taken to be equal to the bootstrap current, as calculated using the Sauter collisional model [19]. In the core, where details of the current are relatively unimportant, the profile is taken to have a simple polynomial form, with coefficients chosen to give a central $q_0=1.05$, and the desired I_p. A number of simplifications are made to streamline the equilibrium construction process, including up-down symmetry (while matching the given separatrix elongation and triangularity), and lack of true X-points.

A first set of model equilibria are constructed to study trends in the pedestal temperature as the density is varied. To allow comparison with a number of shots in the DIII-D database, values of $B_t=2$T, $I_p=1.225$ MA, R=1.685m, a=0.603m, $\kappa=1.77$, $\delta=0.0$ are used. The pedestal width on the outboard midplane is taken to be 1.7cm. The pedestal density is then varied from $2\text{-}9\bullet 10^{19}$m^{-3}, and at each value of the pedestal density, the pedestal temperature is increased until stability limits are reached. Pedestal stability is calculated using the ELITE code. A sampling of wavelengths, n=8,10,15,20,30,40, are studied, over the range expected to be most unstable. A finite growth rate threshold ($\gamma/\omega_A>0.01$) is used as a threshold for "instability," eliminating slow growing modes unlikely to trigger ELMs. We note that the results presented here and in the following section required the production of more than 1000 high resolution 2D equilibria, and more than 6000 intermediate-n MHD stability calculations, but that the efficiency of the ELITE code combined with modern workstation computers make such calculations feasible. The calculated stability limits on T_{ped} as a function of n_{eped} are shown by the solid line in Fig. 5a.

In order to compare the calculated stability curve with observations, we use the DIII-D pedestal database, which contains information on pedestal temperature, density, and width from fits of high resolution Thomson data to a hyperbolic tangent function [3]. The database

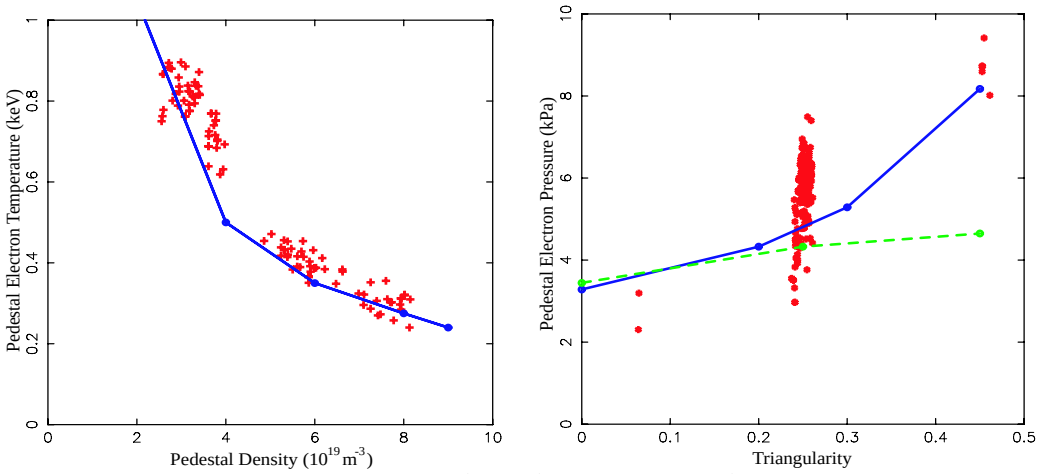

Figure 5: Comparison of calculated pedestal stability boundaries to observed trends in the DIII-D database. (a) The calculated maximum stable pedestal temperature as a function of density (solid line), is compared to the observed variation in pedestal temperature with density during the last 20% of the ELM cycle (asterisks). (b) The calculated maximum stable pedestal pressure as a function of triangularity (solid line) is compared with data (asterisks). The calculated stability boundary with the bootstrap current artificially set to zero is shown by the dashed line.

contains information on more than 20000 time slices from numerous shots, which can then be appropriately filtered, to allow comparisons with trends calculated using model equilibria. Here we select timeslices which are in the final 20% of the type I ELM cycle, with B_t=1.9-2.05 T, I_p=1.15-1.25 MA, δ<0.2, temperature and density pedestal widths between 1.2 and 2.2cm, and injected power P_{inj}>1MW. The data are plotted in Fig. 5a, and provide a reasonable fit to the calculated stability limits, suggesting both that the pedestal is limited by MHD stability in the experiments and that the model equilibria are sufficiently realistic to capture the observed trends.

It is also of interest to study how the pedestal height varies with plasma shape, for example the triangularity (δ). For this purpose we construct a set of model equilibria with B_t=2.08 T, I_p=1.525 MA, κ=1.8, $n_{eped}=4\bullet10^{19}$m^{-3}, and temperature and density pedestal width of 1.4cm. The triangularity is then varied from 0 to 0.45, and at each value, the pedestal temperature is increased until stability limits, calculated as in the previous case, are reached. The resulting stability boundary is plotted in Fig. 5b. The result is again compared to filtered data, here with B_t=2.05-2.15 T, I_p=1.4-1.65 MA, $n_{eped}=3.5\text{-}4.5\bullet10^{19}$m^{-3}, and temperature and density pedestal widths between 0.9 and 1.9cm. The observed strong increase in pedestal pressure with triangularity is consistent with the stability calculations. Physically, the stability limit increases due to increasing second stability access to high n modes as shown schematically in Fig. 2b, with the most unstable mode dropping from n>~40 at δ=0 to n~10 at δ=0.45. The role of the bootstrap current is crucial here. In the absence of bootstrap current, second stability access is not opened and the increase in maximum stable pedestal pressure with triangularity is much weaker, as shown by the dashed line in Fig. 5b. We note that this result is consistent with the observed trend that at high collisionality, where the bootstrap current is strongly reduced, the variation in pedestal height with triangularity is observed to be much weaker.

In Fig. 5, there is of course significant variation in the observed data, even when filtered, as there are a number of parameters which are not tightly controlled by the limited filtering. Furthermore the profile and shape details in the actual shots are only approximately captured in the model equilibria. However, it is quite encouraging that general trends in pedestal height appear to be predictable using model equilibria which approximately match the most important characteristics (eg, B_t, I_p, $\langle n_e \rangle$, κ, δ, Δ), and a bootstrap current model for the pedestal current (which is not accurately measured in present experiments). This result encourages the use of this technique to project approximate pedestal constraints that are expected to pertain in Next Step burning plasma devices, as discussed in the following section.

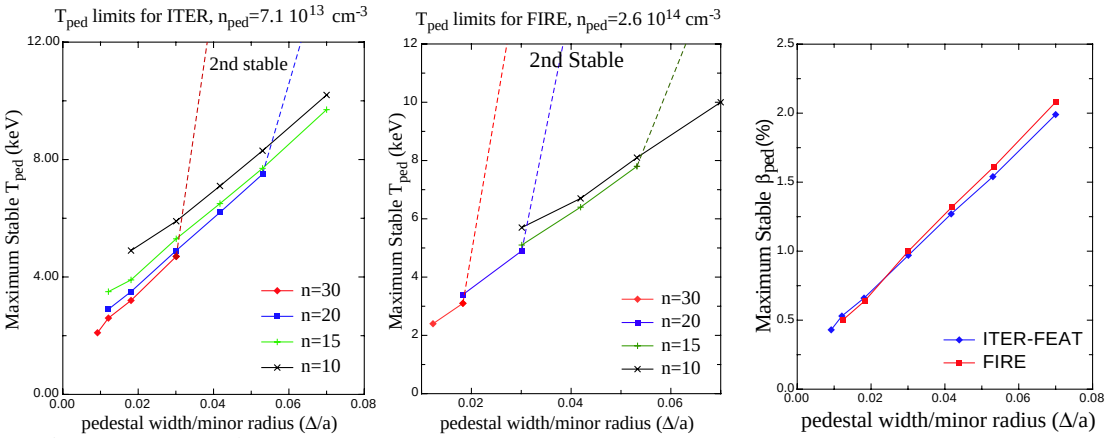

Figure 6: Maximum stable pedestal temperature as a function of normalized pedestal width shown for a range of mode numbers in (a) ITER and (b) FIRE. In both cases, high-n modes become second stable for wide pedestals. (c) comparison of ITER and FIRE pedestal stability limits in terms of the pedestal β.

3.3 Prediction of Pedestal Constraints in ITER and FIRE

The need to attain a high pedestal for good confinement, while operating with sufficiently small ELMs to mitigate erosion of plasma facing components, is especially important to the successful operation of planned burning plasma experiments such as ITER and FIRE. While uncertainty in pedestal transport, in particular the inability to predict the expected pedestal width, makes pedestal prediction challenging, the methods of the previous section can nonetheless be used to calculate the pedestal constraints imposed by stability as a function of the pedestal width and other plasma parameters.

Model equilibria are constructed as in the previous section with reference values of B_t=5.3 T, I_p=15 MA, R=6.2m, a=2.0m, κ=1.85, δ=0.49 and $\langle n_e \rangle = 1.0 \cdot 10^{20} m^{-3}$ for ITER, and B_t=10 T, I_p=7.7 MA, R=2.14m, a=0.595m, κ=2.0, δ=0.7 and $\langle n_e \rangle = 3.6 \cdot 10^{20} m^{-3}$ for FIRE. To characterize the pedestal stability constraints, the pedestal width (Δ) is varied, and at each value of Δ, the pedestal temperature is increased incrementally (with the bootstrap current calculated self-consistently) until stability boundaries are crossed. Results are summarized in Fig. 6. Note that while the maximum stable pressure increases with pedestal width, the dependence is sub-linear, i.e. a higher gradient can be achieved for narrower pedestals. This is because finite-n modes are sensitive to the change in profiles across the pedestal, not just to the local gradient, and because shear increases as the width decreases. More details of the ITER/FIRE pedestal stability study, including studies of variation with triangularity and density can be found in Ref [20].

4. Summary and Discussion

We propose a model for ELMs and constraints on the pedestal based on MHD stability of intermediate wavelength peeling-ballooning modes, which are driven unstable by the sharp pressure gradient and resulting bootstrap current in the pedestal region. The current plays a key dual role in the stability physics, on the one hand providing drive for peeling modes, while on the other hand lowering magnetic shear and, in the presence of shaping, allowing access to second stability for short wavelength instabilities. Field line bending stabilizes long wavelength modes, while short wavelengths are stabilized by a combination of second stability and FLR/diamagnetic effects. As a result, peeling-ballooning mode of intermediate wavelengths (typically n~4-40) are often the limiting instability. The peeling-ballooning stability constraints imposed on the pedestal height are separate functions of density and temperature, due to the collisionality dependence of the bootstrap current, and are in general strong functions of the plasma shape and pedestal width, though not simply linear with pedestal width.

A new MHD stability code, ELITE, has been developed to allow efficient evaluation of stability bounds, growth rates, and mode structures of intermediate wavelength instabilities

in the pedestal region. ELITE calculations allow quantitative study of stability constraints on the pedestal, and together with analytic insight lead to a model of various types of small and large ELM cycle.

Stability calculations on reconstructed experimental equilibria from multiple machines consistently find that peeling-ballooning mode growth rates rise to significant values just before ELMs occur. Parametric studies using series of model equilibria indicate that observed trends in pedestal height with density and triangularity can be explained by peeling-ballooning stability, and confirm the important role of the bootstrap current in pedestal stability. Model equilibria are also employed to study pedestal constraints in planned burning plasma experiments.

A number of additional effects, including diamagnetic stabilization, sheared rotation, and ExB flows, as well as nonlinear dynamics should be considered for a fully quantitative model of ELMs and pedestal constraints. Simple models of diamagnetic stabilization (e.g. $\gamma_{MHD}>\omega_*/2$) can be used to approximately assess its importance in various regimes [20]. Work is ongoing on including additional physics into ELITE, and simulations have been carried out with the nonlinear Braginskii-based BOUT code with current added [21] to allow more physically complete understanding. Preliminary results suggest that the linear behavior of peeling-ballooning modes is similar in ELITE and BOUT.

The level of agreement between the model and observations in both shot by shot comparisons and parameter scans is strongly encouraging, and suggests that a database or parametric fit of pedestal stability constraints as a function of key parameters should be a useful predictive and interpretive tool. Key extensions planned for the model include adding additional physics, comparing to a broader range of experiments, and developing a pedestal stability database.

Acknowledgments Work supported by U.S. Department of Energy under Grant DE-FG03-95ER54309 and Contracts DE-AC0399ER54463, W-7405-ENG-48, and DE-AC05-00OR22725, and by the UK Dept. of Trade and Industry and EURATOM.

References

[1] Hubbard, A.E., Plasma Phys. Control. Fusion 42 (2000) A15
[2] Hatae T., Sugihara, M., Hubbard, A.E., Nucl. Fusion 41 (2001) 285
[3] Osborne, T.H., et. al, Plasma Phys. Control. Fusion 42 (2000) A175
[4] Waltz, R.E., et al, "Performance of Burning Plasma Experiments," Snowmass Meeting, July 2002, http://web.gat.com/snowmass/working/mfe/physics/p4/
[5] Zohm, H., Plasma Phys. Contol. Fusion 38 (1996) 105
[6] Connor, J.W., Plasma Phys. Control. Fusion 40 (1998) 191
[7] Suttrop, W., Plasma Phys. Contol. Fusion 42 (2000) A1
[8] Lao, L.L., Plasma Phys. Control. Fusion 42 (2000) A51
[9] Snyder, P.B. and Wilson, H.R., Contrib. Plasma Physics 42 (2002) 258.
[10] Connor, J.W., *et al*., Phys. Plasmas, **5** 2687 (1998).
[11] Snyder, P.B., Wilson, J.R. Ferron et al., Phys. Plasmas **9** (2002) 2037.
[12] Wilson, H.R., Snyder, P.B., et al., Phys. Plasmas **9** (2002) 1277.
[13] Bernard, L.C., et. al, Comp. Phys. Commun. 24 (1981) 377.
[14] Wilson, H.R., Snyder, P.B., et al., EPS Madeira (2001).
[15] Petrie, T.W., et al., "The Role of Magnetic Balance on the Poloidal Distribution of ELM-induced Peak Particle Flux at the Divertor Targets," submitted to Phys. Rev. Lett (2002).
[16] Leonard, A.W., et al., this conference.
[17] Mossessian, D., Snyder, P.B., Greenwald, M., et al, Plasma Phys. Control. Fusion 44 (2002) 423-437.
[18] L.L. Lao, Y. Kamada, T. Okawa, et al., Nucl. Fusion 41 (2001) 295.
[19] Sauter, O., Angioni, C., and Lin-Liu, Y.R., Phys. Plasmas 6 (1999) 2834.
[20] Snyder, P.B., Wilson, H.R. to be submitted to Plasma Phys. Control. Fusion (2002). P.B. Snyder, et al., Snowmass Meeting, July 2002, http://web.gat.com/snowmass/working/mfe/physics/p3/summaries/snyder_pedestal.pdf
[21] Xu, X.Q., et al., New J. Phys. 4 (2002) 53.